Geodetic evidence for en echelon dike emplacement and concurrent slow slip during the June 2007 intrusion and eruption at Kīlauea volcano, Hawaii

E. K. Montgomery-Brown,[1] D. K. Sinnett,[1] M. Poland,[2] P. Segall,[1] T. Orr,[2] H. Zebker,[1] and A. Miklius[2]

[1]   A series of complex events at Kīlauea Volcano, Hawaii, 17 June to 19 June 2007, began with an intrusion in the upper east rift zone (ERZ) and culminated with a small eruption (1500 m^3). Surface deformation due to the intrusion was recorded in unprecedented detail by Global Positioning System (GPS) and tilt networks as well as interferometric synthetic aperture radar (InSAR) data acquired by the ENVISAT and ALOS satellites. A joint nonlinear inversion of GPS, tilt, and InSAR data yields a deflationary source beneath the summit caldera and an ENE-striking uniform-opening dislocation with ~2 m opening, a dip of ~80° to the south, and extending from the surface to ~2 km depth. This simple model reasonably fits the overall pattern of deformation but significantly misfits data near the western end of an inferred dike-like source. Three more complex dike models are tested that allow for distributed opening including (1) a dike that follows the surface trace of the active rift zone, (2) a dike that follows the symmetry axis of InSAR deformation, and (3) two en echelon dike segments beneath mapped surface cracks and newly formed steaming areas. The en echelon dike model best fits near-field GPS and tilt data. Maximum opening of 2.4 m occurred on the eastern segment beneath the eruptive vent. Although this model represents the best fit to the ERZ data, it still fails to explain data from a coastal tiltmeter and GPS sites on Kīlauea's southwestern flank. The southwest flank GPS sites and the coastal tiltmeter exhibit deformation consistent with observations of previous slow slip events beneath Kīlauea's south flank, but inconsistent with observations of previous intrusions. Slow slip events at Kīlauea and elsewhere are thought to occur in a transition zone between locked and stably sliding zones of a fault. An inversion including slip on a basal decollement improves fit to these data and suggests a maximum of ~15 cm of seaward fault motion, comparable to previous slow-slip events.

1. Introduction

[2]   An intrusion in Kīlauea Volcano's east rift zone (Figure 1) began at 1216 UTC (0216 HST; HST = UTC-10) on 17 June 2007. This intrusion, the fourth in a series of small intrusions [*Heliker and Mattox*, 2003] since the installation of continuous GPS at Kīlauea in 1996, was observed in unprecedented detail by the Global Positioning System (GPS), tiltmeters, and interferometric synthetic aperture radar (InSAR). The intrusion culminated in the

eruption of ~1500 m^3 of lava from a vent near Makaopuhi Crater (~6 km west of the ongoing effusive eruption at Pu'u 'Ō'ō and ~13 km southeast of the caldera). The eruption was not directly observed, but occurred sometime in the early hours of 19 June UTC. Although small in erupted volume, the event significantly disrupted Kīlauea's magmatic plumbing system, and led to ~80 m of crater floor subsidence at Pu'u 'Ō'ō and a temporary cessation of eruptive activity there [*Poland et al.*, 2008a]. Eruptive activity resumed at Pu'u 'Ō'ō on 1 July.

[3]   In addition to the magmatic events, far-field GPS and tiltmeter measurements on the distal flanks suggest concurrent south flank deformation [*Brooks et al.*, 2008; *Montgomery-Brown et al.*, 2007] similar to previously observed slow slip events [*Cervelli et al.*, 2002b; *Brooks et al.*, 2006; *Segall et al.*, 2006]. In this paper we test a

[1]Department of Geophysics, Stanford University, Stanford, California, USA.
[2]U.S. Geological Survey, Hawaiian Volcano Observatory, Hawai'i National Park, Hawaii, USA.
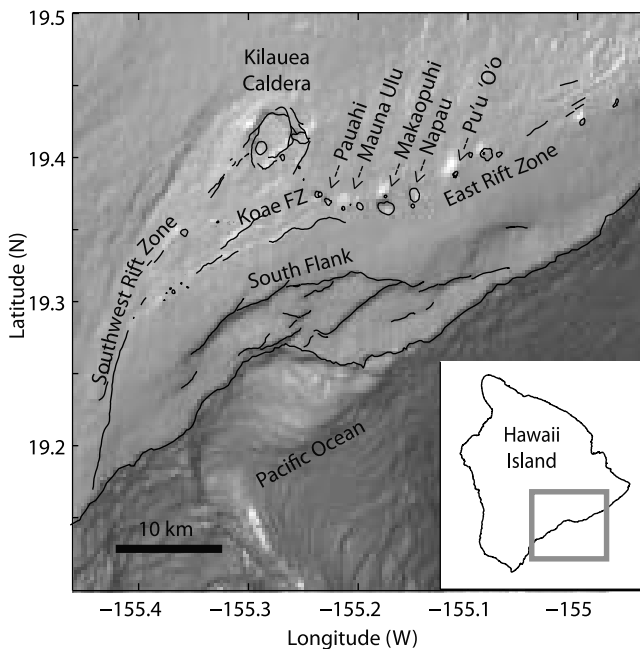
Figure 1. Reference map of Kīlauea Volcano. The major structural features that are referred to in the text are labeled. Inset indicates position of map on the Island of Hawai'i. Annotations and lines indicating the structural features simplified on subsequent maps are overlain on a combined bathymetry and topography map of Kīlauea Volcano from NOAA data.

spectrum of different models of the event, including magma reservoir deflation and dike opening, as well as slip on a possible decollement beneath Kīlauea, to better constrain the deformation sources. For simplicity, we refer to this entire complex event as the "intrusion" throughout this paper.

1.1. Geologic Setting

[4] The major structural features of Kīlauea include a summit caldera and two radial rift zones extending to the southwest (SWRZ) and east (ERZ) (Figure 1). Deformation at the summit caldera can be characterized by inflation and deflation cycles associated with a shallow magma reservoir [*Dvorak and Dzurisin*, 1997]. With the exception of three brief inflationary periods associated with changes in vent geometry at Pu'u 'Ō'ō, the summit subsided continuously between 1983 and 2003, after which it began uplifting [*Miklius*, 2005; *Poland et al.*, 2008a]. The ERZ undergoes persistent extension due to intermittent magmatic events and southward motion of the volcano's south flank [*Owen et al.*, 2000a]. Motion of the south flank is likely accommodated by slip along a basal decollement, interpreted as the interface between seafloor sediments and the overlying volcanic pile [e.g., *Nakamura*, 1980; *Got and Okubo*, 2003; *Morgan and McGovern*, 2003]. Quasi steady state deformation during the 1990s is well-modeled by almost 0.001 km³/yr of summit deflation, 20–30 cm/yr of slip on the decollement, 20 cm/yr of opening in the deep (below ~2 km) ERZ, and 12 cm/yr of left-lateral strike-slip in the upper ERZ [*Owen et al.*, 2000a].

[5] Recent upper ERZ intrusions (e.g., January 1997 [*Owen et al.*, 2000b] and September 1999 [*Cervelli et al.*,

2002a]) manifested as swarms of shallow seismicity accompanied by rapid rift extension and summit subsidence. Despite lava erupting from six distinct surface fissures [*Thornber et al.*, 2003], [*Owen et al.*, 2000b] found that geodetic data associated with the 1997 intrusion could be well-fit by a single, shallow (bottom depth < 2.5 km), steeply southward-dipping dike. A similar model was found for the September 1999 intrusion [*Cervelli et al.*, 2002a]. These events were associated with cessation of eruptions at Pu'u 'Ō'ō for 24 and 11 days, respectively, the longest such pauses in the Pu'u 'Ō'ō–Kupaianaha eruption since the beginning of continuous effusion in 1986 [*Heliker and Mattox*, 2003]. A third recent intrusion, for which geodetic data have not yet been modeled, occurred in 2000 [*Heliker and Mattox*, 2003; *Miklius et al.*, 2005].

[6] While these recent intrusions have been modeled as single segments, Kīlauea's east rift zone has a long history of hosting en echelon eruptive fissures [*Holcomb*, 1987]. En echelon fissures have been shown to result from the opening of cracks in a host rock subjected to both mode I opening and mode III shear [*Delaney and Pollard*, 1981; *Pollard et al.*, 1982], perhaps reflecting the interaction of regional and local stresses. En echelon dikes have been observed at many active and exhumed volcanoes worldwide [e.g., *Delaney and Pollard*, 1981; *Cayol and Cornet*, 1998; *Day et al.*, 1999; *Poland et al.*, 2008b].

[7] The south flank of Kīlauea also hosts aseismic slip events, first noted by *Cervelli et al.* [2002b]. Since then a total of 8 slow slip events have been identified between 1998 and 2007; the most recent prior to 2007 occurred in January 2005 [*Brooks et al.*, 2006; *Montgomery-Brown et al.*, 2009]. Slow slip events observed on Kīlauea, and in subduction zones worldwide [*Schwartz and Rokosky*, 2007], are thought to occur at the transition between a locked zone of a fault and a zone that stably slides. While the mechanics of slow slip are not agreed upon, a number of factors suggest low effective normal stresses in areas where slow slip occurs [*Shelly et al.*, 2006; *Liu and Rice*, 2007].

[8] Past slow slip events released equivalent strain to regular earthquakes ranging from M_w 5 to M_w 6 over the course of 36–48 h [*Montgomery-Brown et al.*, 2009]. The four most similar slow slip events appear to exhibit a 2.1 year periodicity [*Brooks et al.*, 2006]. At the time of publication of the work by *Brooks et al.* [2006], this observation led to the anticipation of an event in March 2007 and prompted the collaborative deployment of additional seismic instruments, two south flank tiltmeters, and an augmented GPS array in early 2007 by the University of Hawai'i, the University of Wisconsin, the Hawaiian Volcano Observatory (HVO), and Stanford University.

1.2. Event Chronology

[9] The June 2007 intrusion occurred in four distinct pulses (noted by times A, B, C, and D in Figure 2) that were distinguished in the seismic and geodetic records [*Wilson et al.*, 2007; *Poland et al.*, 2008a]. The intrusion began on 17 June, 1216 UTC (A in Figure 2) with an earthquake swarm centered 1.5–2 km southwest of Mauna Ulu. More than 38 earthquakes with M > 2 occurred during the first 2 h of the swarm [*Wilson et al.*, 2007]. Summit deflation and southward tilt at ERZ site ESC began simultaneously with the increase in seismicity, followed minutes later by tilt
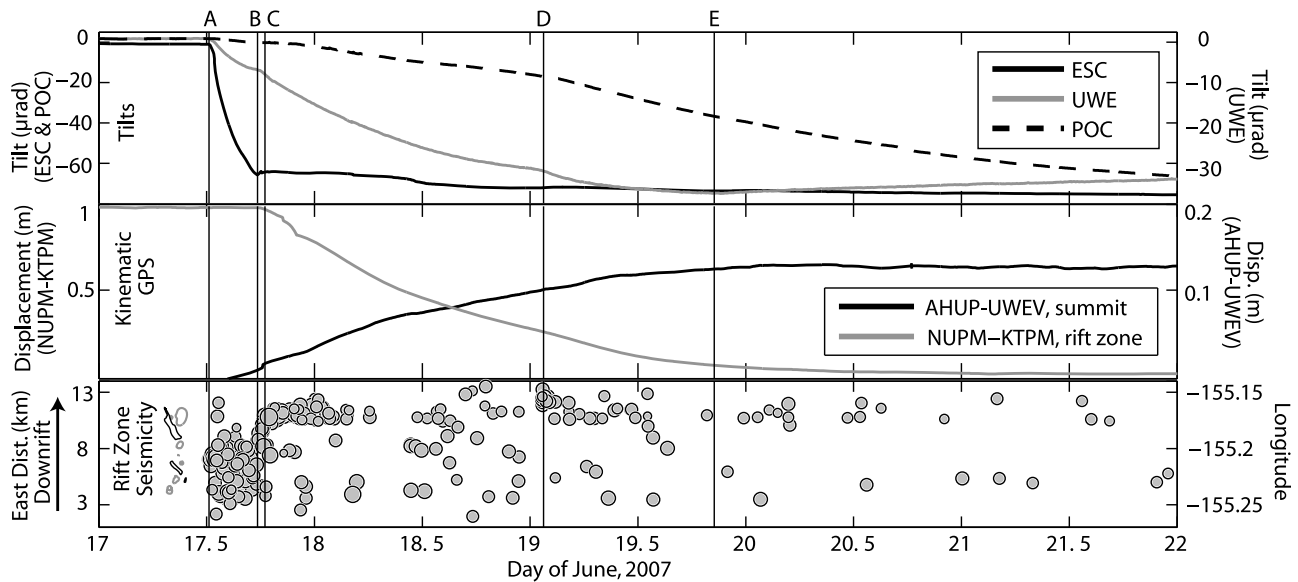
Figure 2. Time history (UTC) of intrusion. (top) North component of ERZ (ESC), summit (UWE), and Pu'u 'Ō'ō (POC) tilt. A negative tilt indicates tilt to the south. (middle) Line length changes between pairs of summit and ERZ GPS stations, kinematically processed for 4 minute positions (note that kinematic data provided by K. M. Larson are presented for reference but only daily solutions were used in this study). (bottom) Space-time distribution of catalog locations of rift zone seismicity [*Nakata and Okubo*, 2008]. GPS station and tiltmeter locations are shown in Figures 3 and 4, respectively. Summit GPS displacements and tilts are scaled to aid in comparing event timings; applicable scales are labeled on the left and right vertical axes. Vertical bars indicate the following events discussed in the text: A, 1216 UTC, ESC and UWE tilt begins with onset of seismicity; B, 1740 UTC, ESC tilt flattens, seismicity concentrates down-rift; C, 1900 UTC, seismicity concentrates down-rift, summit tilt rate increases; D, 0115 UTC, slight increase in tilt rate at UWE and down-rift concentration of seismicity; and E, 2030 UTC, summit tilt returns to inflation.

changes at Pu'u 'Ō'ō. Over the next 5.5 h, the tiltmeter ESC in the ERZ (Figure 2) accumulated ~70 μrad of southward tilt. Seismicity then concentrated down-rift coinciding with an increase in summit tilt rates (1740 UTC, B in Figure 2), the onset of rift zone extension between GPS stations KTPM and NUPM (which span the ERZ near Makaopuhi crater), and slowing of tilt at ESC.

[10] Seismicity propagated down-rift between 17 June, 1900 UTC (time C) and 19 June, 0115 UTC (time D), shown in the space-time distribution of seismicity in Figure 2. Note that seismicity rates had slowed to 3 locatable events per hour after 17 June, 2400 UTC. During this time, the tiltmeter at Pu'u 'Ō'ō (POC) recorded steady tilt toward the crater. The summit and Pu'u 'Ō'ō continued to subside at a diminishing rate up to 19 June, 0115 UTC (D in Figure 2) when summit and Pu'u 'Ō'ō tilt rates increased slightly coinciding with the final down-rift migration of seismicity. The same pattern is observed in the baseline length between KTPM and NUPM. Summit subsidence and rift zone extension continued at diminishing rates until 19 June, 2030 UTC (E in Figure 2), when the summit returned to inflation. Tiltmeter POC continued to record deflation at Pu'u 'Ō'ō, however, until 27 June.

[11] Cracks developed at multiple locations in the ERZ, and steam vents formed along the western base and slope of Kāne Nui o Hamo. On the morning of 19 June, at the eastern end of the cracked zone, HVO geologists observed that a

small amount of fresh lava had been erupted overnight on the north flank of Kāne Nui o Hamo. At Pu'u 'Ō'ō, a lack of lava at the surface by 19 June indicated a pause in the eruption that lasted until 1 July. The pause was likely caused by the interruption of the magma supply to the vent.

2. Data

[12] The Hawaiian Volcano Observatory (HVO), in conjunction with Stanford University and the Pacific GPS Facility of the University of Hawai'i, operates an array of continuous GPS stations on Kīlauea Volcano. The tiltmeter network on Kīlauea is also operated by HVO, with two new sites installed in anticipation of an early 2007 slow slip event. The tilt and GPS instruments provide detailed temporal information on magmatic and tectonic deformation at Kīlauea but are spatially sparse. Temporally sparse, but spatially dense, coverage of deformation is provided by InSAR data from multiple satellites. All of these geodetic data sets have been transformed into a local Cartesian coordinate system with an origin at GPS site MANE (−155.273, 19.339). We have analyzed these various data sets together: three components of displacement from 40 GPS sites, line-of-site (LOS) displacements from three InSAR images, and two perpendicular components of tilt from nine tiltmeters.
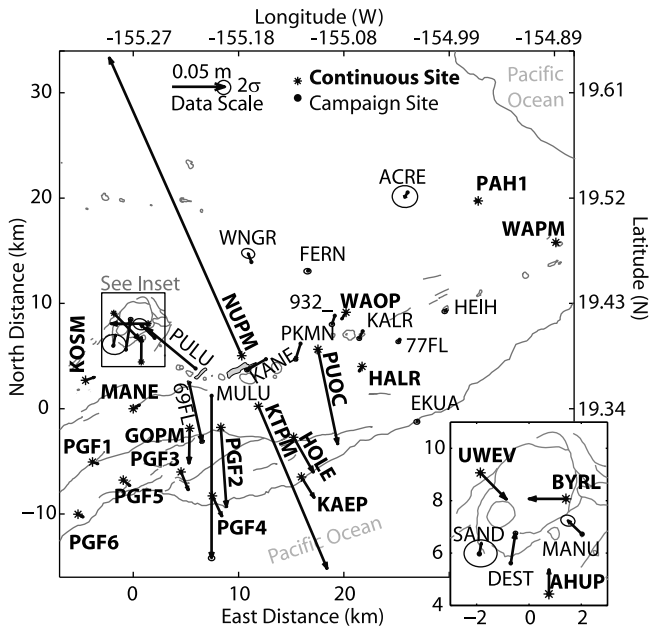
Figure 3. GPS displacements with 95% confidence ellipses. Many ellipses are smaller than the arrowheads. Continuous station locations are marked by an asterisk and bold typeface. Eruption site and steaming areas are outlined in heavy gray (near GPS station PULU and between NUPM and KTPM). Continuous GPS displacements are calculated for a time period between 1 January 2007 and 1 July 2007 using a least squares inversion for displacements (equation (2)). Campaign displacements are calculated from the pre- and post-intrusion 2007 campaigns. See text for processing details. The origin of the local Cartesian coordinate system is station MANE (−155.273°E, 19.339°N).

2.1. GPS

[13] Daily GPS solutions are computed at HVO using the GIPSY/OASIS II software package developed at the Jet Propulsion Laboratory (JPL) in precise point positioning mode with non-fiducial orbits [*Gregorius*, 1996; *Zumberge et al.*, 1997]. The daily non-fiducial solutions are transformed into a global ITRF2005 reference frame [*Altamimi et al.*, 2007] with a 7-parameter Helmert transformation provided by JPL. Since the GPS solutions are tightly constrained in GIPSY, the output formal errors are unrealistically small (10^{-5}–10^{-6} m). We therefore scale the output covariance matrices by 10^3 which retains the relative error information but makes the diagonal elements of the covariance the same order of magnitude as the average standard deviations of the time series (E − 0.003 m, N − 0.002 m, U − 0.015 m, computed from 2 weeks of data during a geodetically quiet period).

[14] Outliers, daily reference frame realization errors, and average velocities are regularly estimated from the entire available set of GPS data from HVO. Outliers – defined as any daily position that is more than 10 cm higher or lower than the mean of that station's position for a 5 day window – are removed from the continuous time series. For example, an outlier can result when a significant fraction of a day's raw data is missing. This outlier filtering removes only a few

days from the 6 months of continuous GPS data included in this study. An estimated velocity of the Mauna Kea permanent GPS station is also subtracted from all stations to put the displacements in a local (island-fixed) reference frame.

[15] We then use a Kalman filter to estimate and remove an average velocity and daily errors in the reference frame realization using a variation of the observation equation proposed by *Miyazaki et al.* [2003]:

$$\mathbf{X}(t) = \mathbf{X_o} + L(\mathbf{x}, t - t_o) + \mathbf{v}(t - t_o) + F\mathbf{f}(t) + \epsilon, \quad (1)$$

where $\mathbf{X}$ is the daily position of each station, $\mathbf{X_o}$ is initial station position at time t_o, L is a random walk process accounting for local benchmark wobble, $\mathbf{v}$ is a constant station velocity, F is a Helmert transformation, $\mathbf{f}$ is a vector of frame translations and rotations which are modeled as a white noise process, and ϵ is the remaining error. At several points in the time series, steps occur due to geologic (e.g., the current intrusion) or man-made (e.g., equipment changes) events. At these times, we reset the variance of L to a large value, allowing the offsets to occur without influencing the velocity or reference frame terms. The average velocity of each site and reference frame errors estimated by the Kalman filter are then subtracted from the time series.

[16] In June 2007, the Kīlauea GPS network included 16 continuous and 14 campaign stations that were measured before and after the intrusion (Figure 3). Continuous GPS data between 1 January 2007 and 1 July 2007 are used to compute displacements during the intrusion. Most of the campaign measurements spanning the intrusion contain little secular deformation, since the 2007 Kīlauea GPS campaign had just been completed before the intrusion. HVO staff were able to quickly re-occupy many sites in the days immediately following the intrusion. Campaign data between 2002 and 2007 are used, with data before 2007 used to constrain site velocities at sites not measured immediately before the 17 June intrusion.

[17] We invert for the GPS displacements spanning the intrusion using a least squares algorithm. Estimated parameters include the pre-intrusion station position $\mathbf{X_o}$, any residual deviations from the previously computed average velocity, $\mathbf{v}t$, and the co-eruptive displacements. Residual velocities are usually very small (<1 cm/yr). Data from 16–20 June 2007, while the intrusion was in progress, are removed in this analysis, as we estimate only the cumulative deformation. The displacement is modeled as a Heaviside function, H, scaled by $\mathbf{d}$, the magnitude of the displacement vector on 20 June 2007:

$$\mathbf{X} = \mathbf{X_o} + \mathbf{v}t + \mathbf{d}H(t_{Jun20}) + \epsilon, \quad (2)$$

where ϵ are the remaining errors. The displacements, $\mathbf{d}$, are analyzed in this study and shown in map view in Figure 3. Several major features of the event are readily apparent in the GPS displacements. First, extension across the ERZ is obvious, particularly the ~0.9 m separation between stations KTPM and NUPM. Second, the summit-area GPS sites displace inward, suggesting summit subsidence. Third, a large signal is seen at PUOC associated with collapse of the Pu'u 'Ō'ō cone.
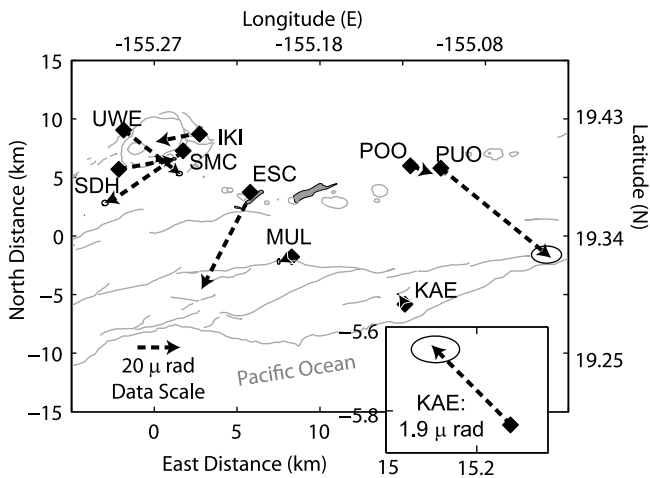
Figure 4. Tilt offsets calculated as the difference in average tilt between 10–13 June and 22–25 June. The 2σ error ellipses are computed from the standard deviations during both time periods; many ellipses are smaller than the arrowheads.

2.2. Tilt

[18] HVO operates a network of electronic borehole tiltmeters around the summit, along the ERZ, and on the south flank (Figure 4). We use data only from tiltmeters that have demonstrated good ground coupling. Because the instruments are emplaced at shallow depths, nearly every tiltmeter exhibits strong diurnal tilts. The magnitude and structure of the diurnal variations depend on local installation conditions.

[19] Tiltmeters are installed in boreholes ~3 m deep and covered, though not sealed, at the surface. The tiltmeter installations record two components of tilt, surface temperature, down-hole temperature, and rainfall once per minute. No rainfall was recorded during the intrusion, simplifying the interpretation of the data.

[20] Daily variations in tilt depend on temperature variations and solid earth tides. Local geology at the site determines the response at each station to temperature and tidal forces. To better discern the magnitude of tilt offsets during the intrusion, we tested several different methods of filtering the diurnal variations before selecting a notch filter as the optimal method.

[21] The filter was designed as a time domain filter with a frequency domain specification. We first removed diurnal periods of 24 ± 3.6 h, which revealed semi-diurnal tidal variations; these were subsequently removed with a notch at 12 ± 3.6 h, resulting in a smooth signal. An example of the pre- and post-filtered tilt series for station KAE is shown in Figure 5.

[22] Cumulative tilts analyzed in the inversions are determined by differencing the 3 day pre-event (10–13 June) average from the 3 day post-event (22–25 June) average. The same time period for each station is used to calculate standard deviations from the means for tilt sites. Several features are immediately obvious in the tilts (Figure 4). Largely inward tilt at the summit indicates caldera subsidence. A large tilt signal is also observed at ESC (~70 μrad of SSW tilt). Near Pu'u 'Ō'ō, POC and POO both tilt toward the

collapsed cone. Lastly, a small, but notable, northwestward tilt occurred at the coastal tiltmeter KAE.

2.3. InSAR

[23] Radar interferograms constructed from data acquired by the ENVISAT ASAR and ALOS PALSAR instruments provide excellent spatial resolution of the deformation field associated with the 17–19 June 2007 intrusion and eruption at Kīlauea. An ascending ENVISAT interferogram (Figure 6a) (12 April to 22 June 2007) and an ascending ALOS interferogram (Figure 6b) (5 May to 20 June 2007) span the intrusion and eruption. GPS results suggest little deformation between 12 April and the onset of intrusive activity on 17 June; therefore, the displacements in the interferograms can be almost totally ascribed to the 17–19 June intrusive and eruptive activity. The ENVISAT radar operates at C-band (5.6 cm wavelength), which does not penetrate vegetation well, and leads to decorrelation in the rain forest north of the ERZ. The ALOS PALSAR has an L-band radar (23 cm wavelength), which better penetrates vegetation, resulting in improved coherence north of the ERZ. An additional descending ALOS interferogram (28 November 2006 to 16 July 2007) is also used in the inversions, although we remove the summit area from our analysis due to uplift suggested in the GPS data in the month following the intrusion (Figure 6c).

[24] Subsequent spatial averaging of the interferograms using a quadtree algorithm reduces the size of the data vector and LOS errors in a statistical sense, but does not reduce any systematic biases. The covariance structure of InSAR measurements, which depends on atmospheric delays, uncompensated topography, and orbit errors, is difficult to model; therefore, we use a diagonal covariance matrix with variances calculated for each quadtree box within the quadtree algorithm [*Welstead*, 1999].

[25] Displacements in the ascending interferograms include LOS lengthening (subsidence) centered near Halema'uma'u Crater in Kīlauea's caldera, as well as two lobes of LOS shortening (uplift), with LOS lengthening in the center along the ERZ near Makaopuhi Crater (Figure 6b). The descending image is dominated by LOS shortening
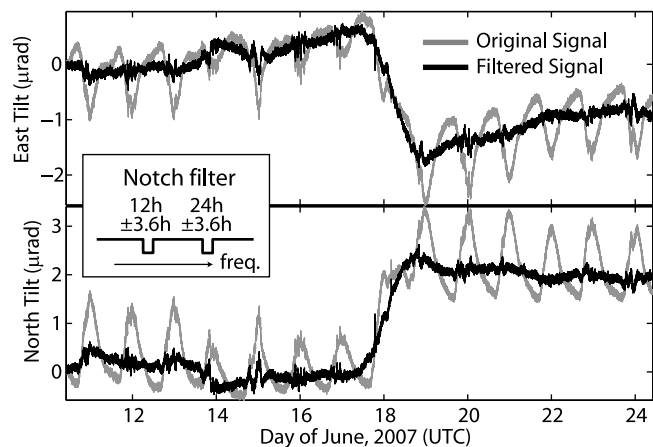

Figure 5. Original east and north components (gray) and notch-filtered output (black) of KAE tilt. Diurnal and tidal frequencies have been removed from the filtered output using notch bandwidths of 3.6 h.
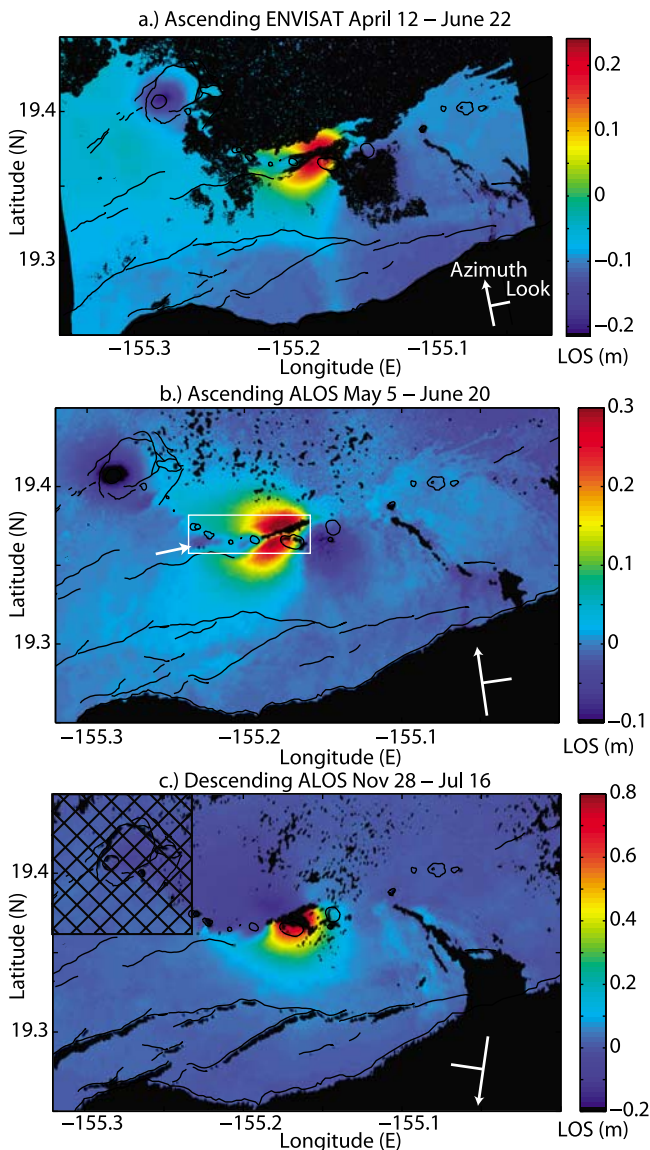
Figure 6. (a) ENVISAT ASAR interferogram spanning 12 April to 22 June 2007 (line of sight (LOS) unit vector: [−0.5463 −0.1088 0.8322]). (b) ALOS PALSAR ascending image spanning 5 May to 20 June 2007 (LOS: [−0.6202 −0.0894 07793]). (c) ALOS PALSAR descending interferogram spanning 28 November 2006 to 16 July 2007 (LOS: [0.6202 −0.0894 07793]). All color scales show LOS displacements in meters. The summit area (cross hatched) of the descending ALOS image (Figure 6c) is not used in inversions because of deformation following the intrusion. The white arrow on the ascending ALOS interferogram (Figure 6b) near the bend in the ERZ identifies the discontinuity discussed in the text, while the white box outlines the area shown in Figure 7.

(upward and southward motion) on the south side of the ERZ (Figure 6c).

2.4. Ground Cracks and Lava Flow

[26] Cracks in the east rift zone above the presumed intrusion were mapped by geologists from the Hawaiian

Volcano Observatory (Figure 7) on 18 June 2007 and subsequent visits to the site. Most cracks occur in a zone ~600 m wide and are oriented ~65°. Both right- and left-stepping cracks were mapped. The crack zone extends down-rift over a distance of 3 km, beginning 1.3 km east of the summit of Mauna Ulu, crossing the north flank of Kāne Nui o Hamo, and extending as far as the eruption site. The western end of the cracked area was examined in more detail, confirming its broad, blunt character. No cracks were observed east of the eruption site.

[27] The area east of Pauahi Crater, along the Nāpau hiking trail, also hosted some cracks oriented 65°, although this zone was much less well developed than the main crack zone to the east. A series of larger, en echelon cracks in this zone cut the Mauna Ulu road and even defined a low hump crossing the pavement (Figure 7).

[28] A final cluster of cracks mapped on the Chain of Craters road were also directly related to the June 2007 event, extending a few hundred meters to either side of the highway (Figure 7). The crack orientations ranged from 90° to 115° and appeared to trend westward into a north-facing normal fault in the Koa'e fault zone that is buried by a 1969 lava flow. Slip on this fault occurred during the September 1999 intrusion [*Cervelli et al.*, 2002a]. The largest of the new cracks in this zone had 2 cm of separation, with a suggestion of south-side-up motion. Measurements of the distance between pins spanning a 5–10 m wide crack at crack station 98-10 (Figure 7) indicate 3.9 ± 0.4 cm of opening between 30 April 2003 and 12 July 2007. Opening at crack station 98-11 was within errors at 0.2 ± 0.4 cm during the same time period. Although this is a long time interval, past measurements at this site have shown little movement except during intrusions, suggesting that much of this measured opening could be attributed to the June 2007 intrusion (D. Swanson, personal communication, April 2009). A campaign GPS site (69FL) and a discontinuity in the ascending ALOS interferogram (Figure 6b) are located nearby and may be affected by this ground cracking. Effects of this normal faulting on the inversions are presented following discussion of the models.

3. Model Inversions

[29] Observed GPS displacement and tilt patterns are similar to previous dike intrusions on Kīlauea [*Owen et al.*, 2000b; *Cervelli et al.*, 2002a], which were modeled as simple uniform-opening dislocations. We therefore begin with a similarly simple model of the event consisting of a Mogi source of volume change [*Mogi*, 1958] and a rectangular dislocation with uniform-opening [e.g., *Okada*, 1985] to model summit deflation and ERZ dike opening respectively. This model, and all subsequent models in this paper, are kinematic and assume an isotropic, homogeneous, linearly elastic half-space. We assume a Poisson's ratio of 0.25 and a shear modulus of 3×10^{10} Pa. All modeled deformations are computed from expressions given by *Mogi* [1958] and *Okada* [1985].

3.1. Optimal Uniform-Opening Dike

[30] To determine constraints on the distributions of possible source parameters, we employ Markov Chain Monte Carlo (MCMC) optimization [*Metropolis et al.*,
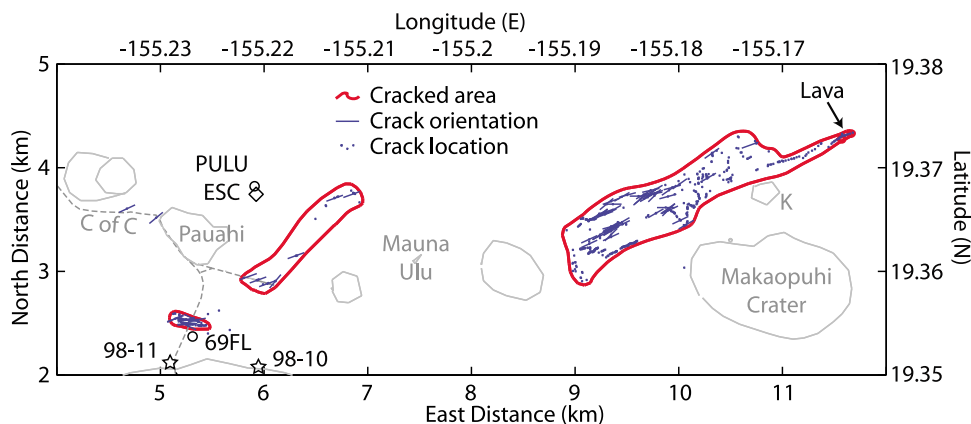
Figure 7. Mapped crack locations (dots) and orientations (small lines). Nearby GPS (PULU and 69FL, marked with circles) and tilt (ESC, marked with a diamond) sites are labeled. PULU and ESC are co-located. Stars mark the location of crack stations 98-10 and 98-11. Just north of Makaopuhi Crater, "K" marks the summit area of Kāne Nui O Hamo lava shield, on which the farthest eastward extent of the surface cracking and the small lava flow were observed. "C of C" marks Chain of Craters Road. The road toward Mauna Ulu ends at the Nāpau trail head. The two small craters on either side of Mauna Ulu have been filled by subsequent lava flows. Direct measurement of the distance between steel pins at crack station 98-10 indicated 3.9 ± 0.4 cm of opening displacement between 30 April 2003 and 12 July 2007. The opening at station 98-11 was 0.2 ± 0.4 cm for the same time period.

1953] to build posterior distributions of the parameters describing an inflating planar dislocation in the rift zone (length, width, depth, dip, strike, east position, north position, and opening) and a deflating Mogi source at the summit (east position, north position, depth, and volume change). The a priori distribution of model parameters is assumed to be uniform between broadly chosen bounds. Since lava was erupted at the surface, we constrain the top of the dike to lie within half a kilometer of the surface. Models with unrealistic aspect ratios, defined by the ratio of the opening to the minimum of the length and the width, are rejected by requiring that the minimum dike dimension be at least 1000 times its opening. This corresponds to a maximum allowed dike pressure on the order of tens of MPa, which is larger than values used for similar modeling [*Yun et al.*, 2006] and thus should allow the MCMC search to sample only dikes with realistic dimensions. The optimum model from a short MCMC search (1 million samples) is used to initiate a thorough search of 10 million samples of the model space. We save every tenth model to avoid correlation between model steps [*Fukuda and Johnson*, 2008].

[31] The optimal uniform-opening dike is sub-vertical (dipping 81° to the south), nearly 4 km in length, and has a width that extends from the surface to a depth of ~1.9 km, with ~1.8 m of opening (Table 1). The modeled dike strikes along observed surface disruptions (the eruption site, ground cracks, and steaming areas) and follows the linear part of the axis of deformation seen in both the ascending ALOS and ENVISAT interferograms (Figure 8). To first order, this model fits the observed GPS displacements, InSAR LOS displacements, and tilt. Despite the overall fit, however, there are several obvious misfits (Figure 8). Predicted tilt at ESC is roughly 90° from observed. Predicted displacements at 69FL are in the opposite direction from the observed, and far smaller in magnitude; this misfit may be a result of motion along the Koa'e fault system near station 69FL. In

addition, predicted displacements at MULU and GOPM are far smaller in magnitude than observed. The summit area GPS sites are also not well fit by this model; predicted displacements show a systematic westward misfit.

[32] Single dislocation models of the dike, while simplistic, do allow us to constrain the range of possible parameters that fit the data. Certain parameters are well constrained, such as the position and length of the dike, which are limited by the down-rift extent of deformation recorded by InSAR, and the westward displacements at campaign GPS sites KANE and PKMN. Somewhat less well constrained are the strike, dip and amount of opening. Ninety-five percent of the models have strikes that range from 55 to 80° (Figure 9). The dips of the dislocation models are defined according to the convention of *Okada*

Table 1. Upper and Lower Bounds of the Uniform a Priori Distribution of the MCMC Model Parameters and 95% Bounds of the Posterior Distributions[a]

Parameter	Lower a Priori	Upper a Priori	Lower 95% Posterior	Upper 95% Posterior	Optimal
		Dike			
Length (km)	0.1	15	0.89	9.3	3.9
Width (km)	0.1	9	0.25	5.5	1.9
Depth (km)	0	9	0.52	5.6	1.9
Dip (degrees)	20	160	70	107	81
Strike (degrees)	20	160	48	84	67
East Position (km)	5	15	9.4	12.1	10.1
North Position (km)	1	9	2.6	4.9	3.3
Opening (m)	0.001	8	1.3	7.8	1.8
		Mogi			
East Position (km)	−2.5	2	−0.9	0.1	−0.9
North Position (km)	5.5	10	6.8	9.9	8
Depth (km)	0.1	15	0.14	4.9	2.5
Volume (m^3)	−1e8	1e4	−1.9e7	−1.2e5	−6e5

[a]The optimal model is defined as the model with the lowest misfit. See text and Figure 12 for parameter definitions.
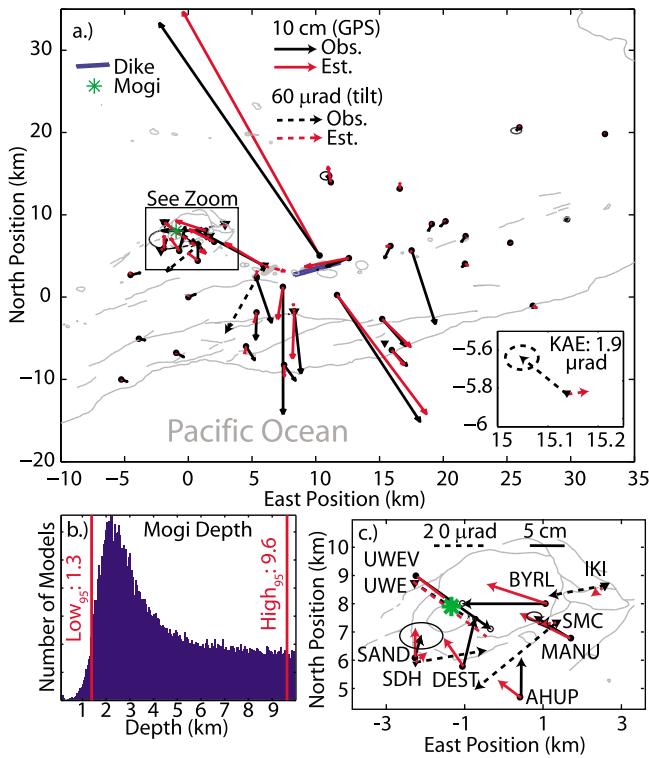
Figure 8. (a) Observed (black) and estimated (red) GPS displacements (solid lines) and tilts (dashed lines) from the optimal uniform-opening dike model. Lava and steaming areas are outlined in heavy gray but are partially covered by the dike. (b) Posterior distribution of depths to the Mogi source with vertical bars indicating upper ("high") and lower ("low") 95% confidence bounds. (c) Kīlauea caldera and the summit area of the map.
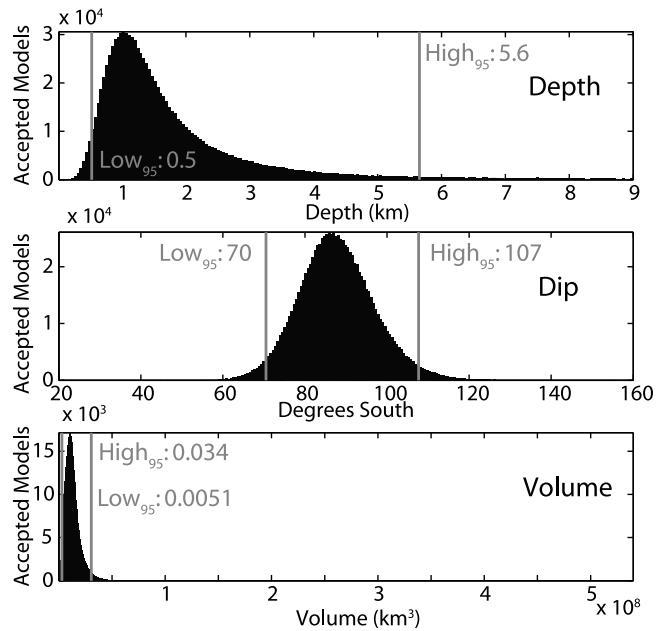

Figure 9. Histograms of depth to the dike bottom, dike dip, and dike volume from 1,000,000 Monte Carlo samples of the model space. Vertical bars indicate upper ("high") and lower ("low") 95% confidence bounds, while the horizontal axis limits are the a priori parameter bounds.

[1985]. A dip of zero is a horizontal plane, a 90° dip is a vertical plane, dips less than 90° are southward, and dips greater than 90° are northward. Acceptable dips are all very steep and range from about 70–107°. The amount of opening ranges from ~1.3 to 7.8 m, and is correlated with the size of the dike (i.e., smaller dikes have more opening), such that dike volume is well-constrained (Figure 9). While useful in constraining dike parameters in a statistical sense, these overly simplistic models are unable to sufficiently fit near-field (within a few dike lengths) data. We thus turn to distributed opening models in section 3.2 and include one model which has a fixed geometry based on the optimal (minimum misfit) MCMC sample (Table 1). In this model, one dike segment's geometry is fixed from the strike, dip, and position of the dike from the optimal MCMC model, while the length, width and depth of the potential source are extended to allow the opening distribution to taper smoothly to zero near the edges.

3.2. Distributed Opening-Dike Models

[33] Three different dike geometries are tested in linear, distributed opening inversions. Mogi sources are also included under the summit and Pu'u 'Ō'ō at depths of 2.5 km and 100 m, respectively. The summit source depth was

determined from the MCMC inversions, while the source beneath Pu'u 'Ō'ō was chosen to be consistent with the depth of open-system degassing [*Edmonds and Gerlach*, 2007]. The three different dike models (Figure 10) are based on particular geologic and geodetic observations and are constructed from uniform-opening rectangular patches ~0.5 km on each side. Noting that the earthquakes associated with this intrusion follow the curve of the east rift zone, we construct the first model, Curving Dike (model 1), following the surface trace of the recently active part of the rift zone marked by spatter cones and pit craters (Figure 1). We construct a second model, Curving Dike (model 2), following the axis of deformation in the ascending ALOS interferogram, which
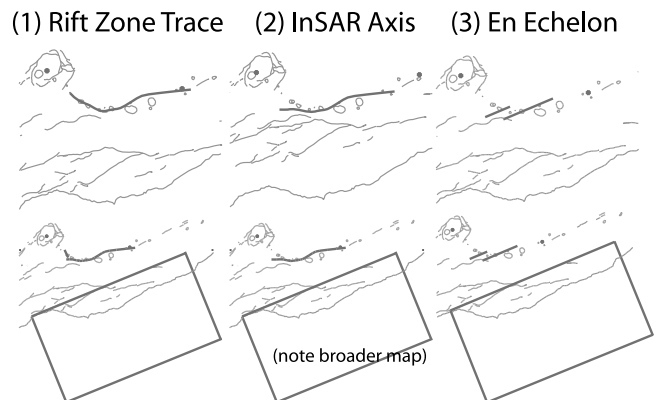

Figure 10. Schematic dike-only models (top) and models including decollement slip (bottom) explored with distributed opening and distributed fault slip. Dots at the summit and Pu'u 'Ō'ō indicate Mogi source positions.
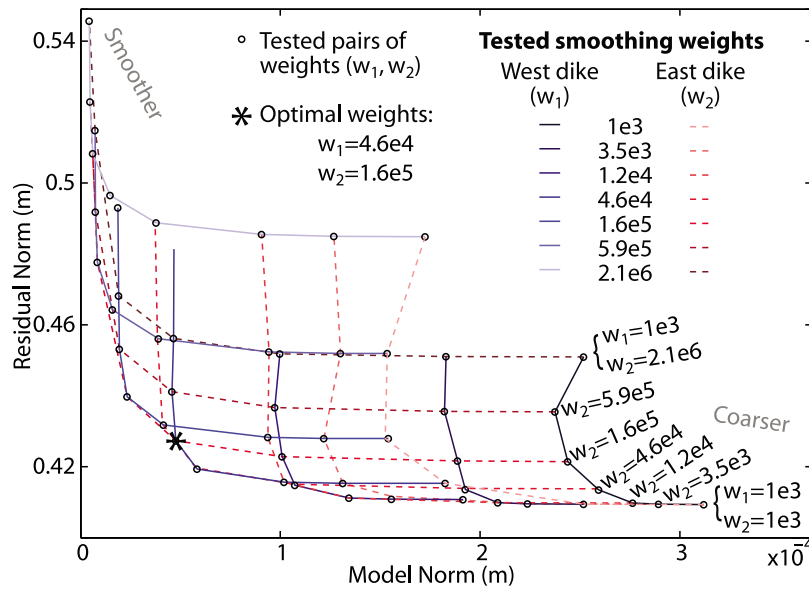
Figure 11. Example L-curves showing the grid search of smoothing parameters for the en echelon dike model. Blue solid lines connect tests using the same value of the smoothing parameter on the western segment (w_1), while red dashed lines connect tests using the same smoothing parameter on the eastern segment (w_2). Each dot represents the test of a pair of parameters from which the model norm and residual norm were calculated. The asterisk marks the pair of weights used in the inversion.

does not follow the surface trace of the rift zone, but instead continues to trend westward after the rift zone curves north toward the summit (Figure 6). The third model (model 3) is a pair of en echelon dikes aligned with mapped areas of surface cracking (Figure 7). En echelon dikes and fissures are commonly observed during rift zone eruptions; examples can be found in Iceland [e.g., *Gudmundsson*, 2003] and in previous eruptions of Kīlauea [e.g., *Fiske and Koyanagi*, 1968]. A small right step (~100 m) in the crack zone was also observed near the small pad of lava at Kāne Nui o Hamo at the far eastern end cracked zone. Because geodetic data are unable to resolve such a small separation, and the InSAR images decorrelate over the dike, none of the models address this level of spatial detail.

[34] The distributed opening inversions are accomplished with a non-negative least squares algorithm that minimizes the L2-norm of the weighted-residuals. Spatial smoothing is applied with a Laplacian operator for each dike segment, with one smoothing parameter each for both curving dike models, and two for the en echelon model (one for each dike). A line search for the optimal smoothing parameter is conducted (grid search of two smoothing parameters in the case of the en echelon dikes), and the optimal weight chosen with the L-curve criteria [*Hansen*, 1992] such that the optimal parameter produces the smoothest model with a minimal increase of the residual norm (Figure 11).

[35] The opening distribution shown in Figure 12 is representative of all three distributed opening models, with a maximum of ~2.4 m of opening between Makaopuhi and Nāpau Craters. A second local maximum opening of nearly 1.6 m occurs near Pauahi Crater. The majority of the modeled opening is concentrated beneath the mapped areas of surface cracking, and opening tapers sharply to zero down-rift of the small pad of lava on Kāne Nui O Hamo (Figure 12).

[36] We use the percentage of data variance:

$$1 - \|d - \hat{d}\| / \|d\|, \tag{3}$$

where d is the data vector and $\hat{d}$ is the model prediction, explained by the model as a measure of misfit. This variance
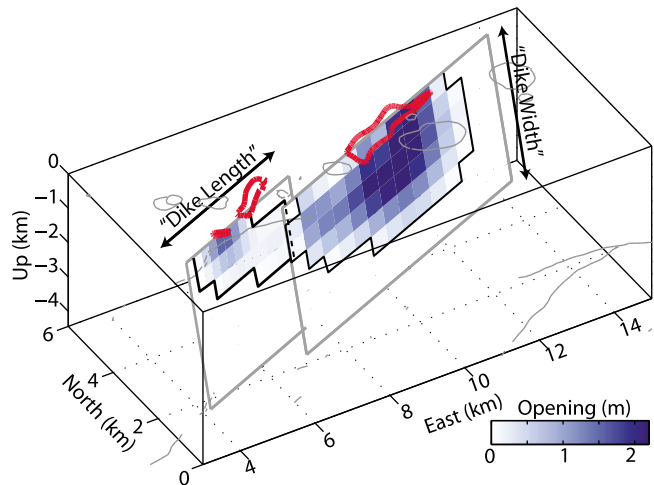

Figure 12. Dike opening distribution from the en echelon model. Arrows labeled "dike length" and "dike width" define the model parameters following *Okada* [1985] . Gray outlines show the model elements that are allowed to open in inversions, while the black outlines enclose the resulting nonzero opening distribution. The intensity of the blue color indicates the amount of opening on that patch of the dike. Without constraint, most opening is located beneath mapped areas of surface cracking.

Table 2. Percentage of the Data Variance Explained by Each Type of Model for the Total Data Set (1172 Data Points), and Individual Subsets[a]

	Dike Only			Dike and Decollement		
Model	Rift Zone	InSAR Axis	En Echelon	Rift Zone	InSAR Axis	En Echelon
Percent variance total	44	88	89	59	78	90
WRMS total	0.93	0.45	0.48	0.94	0.52	0.45
Singular values	83	83	226	283	283	426
Percent variance GPS	82	91	89	85	94	92
Percent variance Tilt	62	61	85	55	62	83
Percent variance SAR	42	88	90	57	78	89

[a]A weighted root-mean square (WRMS) misfit [*Segall and Harris*, 1986] is calculated, which takes into account the degrees of freedom in each inversion.

reduction can be computed for the total data set, as well as for each individual subset of data (GPS, tilt, and InSAR). The variance of the data ($\|\sigma\|/\|d\|$, where σ is the diagonal of the covariance matrix) is about 3.5%.

[37] A weighted root mean square error (WRMS) can also be computed for the total data set following *Segall and Harris* [1986]:

$$\text{WRMS} = \left[\frac{1}{N-P} \sum_{i=1}^{N} r_i^2 w_i^2 \right]^{1/2}, \qquad (4)$$

where N is the number of data (N = 1172), P is the number of degrees of freedom, r is the residual error vector ($d - \hat{d}$), and w are weights determined from the inverse of the covariance. This WRMS takes into account the number of degrees of freedom in each inversion. Although the degrees of freedom are not well defined when the inverse problem is regularized with smoothing and non-negativity constraints, we can make a reasonable estimate by determining the degrees of freedom from the number of significant singular values. These singular values are determined from an SVD of the Green's functions including comparable smoothing, but without non-negativity constraints.

[38] The total percentage of data variance explained by the distributed opening models ranges from 44 to 89%, but individual subsets of the data are better fit than others (Table 2). Particular models, however, also have disqualifying features. Both the model that follows the rift zone and the model that follows the axis of InSAR deformation are unable to reproduce the ~110° difference in the GPS (PULU) and tilt (ESC) directions at the west end of the dike. In fact, neither curving dike produces southward tilts at ESC; both predict northwest tilt. The en echelon model, while not perfectly fitting these two stations, provides a much better fit than either of the curving dike models (Figure 13).

[39] We note that the western en echelon segment is very near the September 1999 dike, but strikes 67° as opposed to 85° [*Cervelli et al.*, 2002a]. We tested models with the western dike segment striking 85° as in the 1999 intrusion. The overall percentage of variance fit by this model, and the percentage of the InSAR variance fit locally near Pauahi Crater are the same as those for the parallel en echelon segments. The 67° strike is preferred here because it is

consistent with the orientation of the cracks observed along the Nāpau trail, and is able to model the ~110° difference in the co-located sites ESC (tilt) and PULU (GPS). The 85° striking dike model is unable to produce the observed northwestward displacement direction at PULU.

[40] As noted in section 2.4, it is possible that slip may have occurred on a north-dipping normal fault in the Koa'e fault zone, as was the case during the 1999 intrusion [*Cervelli et al.*, 2002a]. This hypothesis is supported by the offset seen in the ascending ALOS interferogram near site 69FL (Figure 13) and by cracks observed across Chain of Craters road (Figure 7). To test how the data near the crack zone may have influenced our inversions, we remove GPS site 69FL and InSAR pixels in a 2 km by 1 km box around the Chain of Craters road cracks, and re-invert for the distributed dike opening. Overall percentages of the data variance fit by the models remain the same, but a small volume increase and ~1 km eastward shift of the maximum opening on the western dike segment predict tilts at ESC that are ~30° westward of the observed. The predicted tilt at ESC is still southward and close to the observed magnitude, which neither of the curving dikes can produce.

[41] If we include a steeply north-dipping normal fault at the location of cracks and InSAR phase discontinuity extending from the surface to 1 km deep, inversions estimate ~10 cm of slip on the normal fault. This amount of slip does not significantly influence the predicted tilt at ESC, since it only contributes ~1 μrad while the total observed tilt at ESC was ~80 μrad. A normal fault that breaks the surface has a
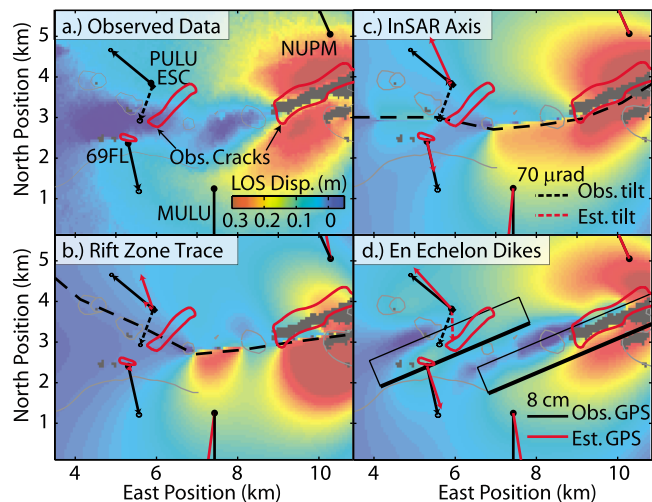

Figure 13. A comparison of model predictions for each of the dike-only models, focused on the near-field deformation. (a) Observed data.; (b) Model 1 following the surface trace of the rift zone (51%). (c) Model 2 following the symmetry axis of the InSAR data (89% of InSAR variance explained by this model). (d) Model 3, a pair of en echelon dikes (89%). The ~110° difference in displacement and tilt directions at co-located GPS site PULU and tilt site ESC are not able to be replicated by curving dike models following either the surface trace of the rift zone or the symmetry axis of the InSAR data. The overall fit is best for the en echelon-arranged displacement sources.
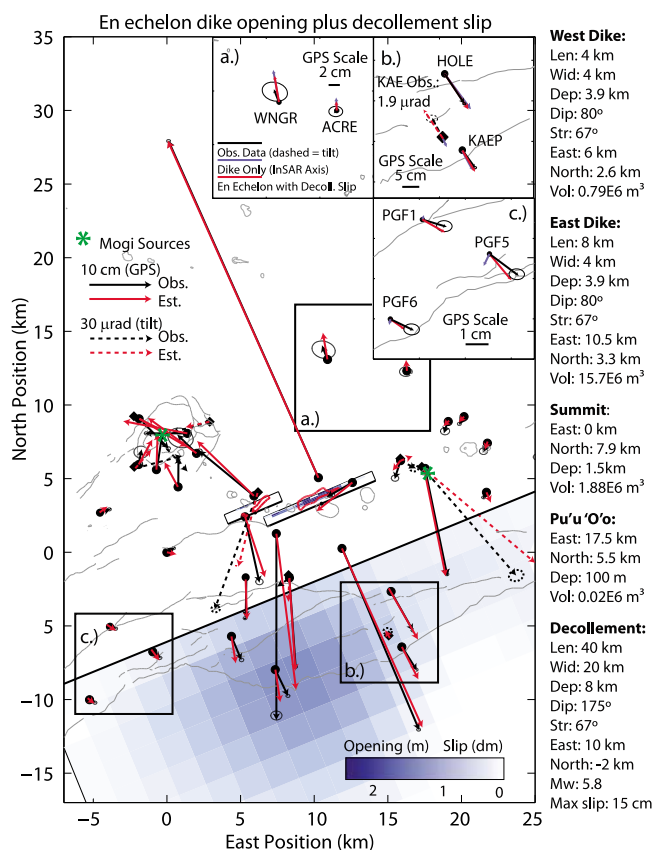
Figure 14. Preferred model of the deformation associated with the 17–19 June intrusion including two en echelon dike segments and decollement slip. Dislocation model parameters represent the full extent of allowed opening in inversions, and are measured from the center of the bottom edge, with length measured along strike and width along dip, which is nearly vertical. Volumes are computed by integrating the distributed opening model, in which many patches, especially deeper patches, have zero opening (see Figure 12). Detail views emphasize local improvements over dike-only models after adding decollement slip: Insets are for a, North flank GPS displacements; b, coastal site KAE; and c, displacements at southwestern flank sites.

very sharp displacement discontinuity, and is too sharp to reproduce the gradient observed in a N–S profile of the InSAR data through the center of the normal fault. Deepening the top of the fault to 50 m below the surface increases the amount of estimated slip to ~20 cm and provides a better fit to the InSAR profile immediately above the normal fault.

[42] Despite including a normal fault, dike opening on the western segment is still required to fit the magnitude of the uplift observed in the InSAR to the north and south of the fault, and the GPS displacements at PULU and 69FL. The presence of the normal fault in the models shifts the optimal location of maximum dike opening on the western segment about 1 km eastward, similar to models where data near the crack zone were removed. Based on this inversion, which included a normal fault, and the previous one, which removed data near the normal fault, the preference for the

overall dike model of two en echelon segments does not change. It is likely, however, that a pre-existing normal fault in the Koa'e fault system above the western segment slipped during the intrusion.

[43] While the en echelon dike model is the best fit to the near-field observations, there are some notable local misfits to all of the dike models: (1) the direction and magnitude of the southwestern flank GPS stations (PGF1, PGF5 and PGF6) (also noted by *Brooks et al.* [2008]), (2) opposite sign of tilt at coastal site KAE, and (3) over-prediction of GPS sites north of the east rift zone. These particular misfits, further detailed in section 3.3, lead us to believe that a dike-only model may not be sufficient to model these data.

3.3. Evidence for Concurrent Slow Slip

[44] When taken together, three main observations suggest that slow flank slip occurred during the June 2007 intrusion including (1) northward tilting at the coastal tilt-meter KAE and coastal subsidence measured by GPS, (2) southeastward displacements at GPS sites on Kīlauea's southwestern flank (PGF1, PGF5, and PGF6), and (3) a small swarm of flank seismicity that, while not uniquely activated during slow slip events [*Montgomery-Brown et al.*, 2009], has accompanied most previous slow slip events [*Wolfe et al.*, 2007].

[45] The tiltmeter KAE, installed at the coast in early 2007 to record an anticipated slow slip event [*Brooks et al.*, 2006], tilted down to the north during the June 2007 intrusive event. Models of typical east rift zone intrusions, and the specific models presented in section 3.2, predict southward tilts at the coast. Tilts predicted by models of the 2005 slow slip event model [*Segall et al.*, 2006], however, do tilt to the north, suggesting that flank slip is required to explain this northward tilt at KAE during the June 2007 event (Figure 14, insets).

[46] During the intrusion, vertical displacements at coastal GPS sites are consistent with the tilt, exhibiting subsidence along the coast, while similarly distant GPS sites to the north of the rift do not. Models of dikes that break the surface produce uplift everywhere, which is inconsistent with the observed south flank subsidence. Offshore decollement slip, however, produces subsidence on the south flank, as observed.

[47] Southeastward displacements at GPS sites in the far western part of the Kīlauea GPS network are consistent with those measured during previous slow slip events [*Brooks et al.*, 2008]. None of the intrusions previously observed by continuous GPS (e.g., 1997, 1999 and 2000) produced significant deformation at these sites, nor do any of the dike-only models discussed as part of this study. While these sites only show very small displacements of <1 cm, displacement signals are above the background noise level (Figure 14, insets a).

[48] In addition, previous slow slip events are associated with a distinct pattern of microearthquakes [*Segall et al.*, 2006; *Wolfe et al.*, 2007]. A similar cluster of micro-earthquakes was observed during the 2007 intrusion, but not during the 1997 and 1999 intrusions [*Brooks et al.*, 2008]. Although the South flank earthquake swarm is suggestive, the south flank is known to be highly active following rift zone intrusions [*Dvorak et al.*, 1986], and this particular cluster of earthquakes is often active without an apparent

trigger [*Montgomery-Brown et al.*, 2009]. Nevertheless, together these observations compel us to test models including dike opening and decollement slip.

3.4. Dike Intrusion and Decollement Slip

[49] Here we examine inversions that include slip on a decollement structure beneath Kīlauea's south flank in addition to the same dike models presented in section 3.2. The sub-horizontal decollement is located at a depth of 8 km coinciding with the planar alignment of decollement earthquakes [*Got and Okubo*, 2003; *Hansen et al.*, 2004] and the inferred depth of the slow slip events [*Segall et al.*, 2006; *Montgomery-Brown et al.*, 2009]. For our models, the decollement plane is divided into a ten-by-twenty grid of fault patches 2 km square. A Laplacian smoothing operator is applied to the dislocation models of the decollement as well as the dikes, and the weights are again determined by the L-curve criteria.

[50] While including the decollement produces minor differences in the dike opening distribution, the major features remain the same with the majority of the opening occurring under the mapped surface cracks. The total estimated dike volume is 16.6×10^6 m^3 (western segment: 0.79×10^6 m^3, eastern segment: 15.8×10^6 m^3). The summit's volume loss is 1.8×10^6 m^3, while Pu'u 'Ō'ō's volume loss is 0.02×10^6 m^3.

[51] As in the 1997 [*Owen et al.*, 2000b] and 1999 [*Cervelli et al.*, 2002a] intrusions, volume loss from the summit does not account for the dike volume. The pair of en echelon dikes constitute a total volume increase of 16.6×10^6 m^3, while deflation at the summit and Pu'u 'Ō'ō magma reservoirs account for a total volume loss 1.82×10^6 m^3. We can estimate the volume of magma drained from the cone of Pu'u 'Ō'ō from the length of time it took for lava to reappear at Pu'u 'Ō'ō (12 days) and the magma supply rate to Kīlauea. During the first twenty years of eruption the magma supply rate was 0.12 km^3/yr [*Heliker and Mattox*, 2003], which is probably a minimum since [*Poland et al.*, 2008a] suggested the magma supply rate had increased between 2003 and 2006. This minimum rate implies that at least 3.65×10^6 m^3 of lava drained from Pu'u 'Ō'ō, giving a ratio of dike volume gain to magma reservoir loss, r_v, of 3.03.

[52] Deeper, geodetically undetectable sources are often called upon to explain volume discrepancies. On Kīlauea, the deep rift zone may be one such source. *Rivalta and Segall* [2008], however, showed that this difference may also be explained by the compressibility of the magma, and the shapes of the magma reservoirs, and dikes. *Rivalta and Segall* [2008] found ratios of dike volume gain to magma reservoir loss, r_v, range between 1.24 and 4.33 based on realistic values of magma compressibility and rock rigidity for Kīlauea, consistent with the values estimated above for the June 2007 event.

[53] Regardless of the details of the dike geometry, maximum seaward decollement slip estimates are ~15 cm with a moment magnitude of $M_w = 5.7$. While the magnitude and location of this event are similar to previous slow slip events, the number of south flank aftershocks is far fewer than similarly sized slow slip events that occurred in the absence of intrusions [*Montgomery-Brown et al.*, 2009]. Slip is concentrated south of the Hilina fault system and close to the coast, as was seen in previous slow slip events [*Montgomery-Brown et al.*, 2009].

[54] In general, models including slip on the decollement result in misfits similar to dike-only models. The total percentage of the data variance explained by models that include the decollement shows slight improvements relative to the dike-only models, but we have also increased the number of free model parameters. Independently, the GPS and InSAR data are each better fit by a few percent (Table 2). As in dike-only models, the en echelon segments are a significantly better fit for the InSAR data.

[55] The fits to particular stations, however, are much improved by including decollement slip. Displacements at stations north of the rift zone are not over-predicted as much as they are with dike-only models (Figure 14, insets a). The modeled tilt at KAE is down to the north when including decollement slip, which does not occur in dike-only models (Figure 14, insets b). Last, modeled GPS displacements at the west flank sites PGF1, PGF5, and PGF6 are oriented to the southeast, consistent with the observations and previous slow slip events (Figure 14, insets c).

4. Discussion

[56] We draw two major conclusions from our modeling of the 17–19 June 2007 Kīlauea intrusion and eruption: (1) two en echelon-arranged dikes provide a much better fit to local surface displacements than curved dike models and (2) the addition of decollement slip is required to fit the far-field displacements resulting from this intrusion.

[57] The en echelon model is consistent with observed locations of surface cracking, steaming areas, and erupted lava, and improves the fit between the model and the near-field surface deformation. Historically, dikes and cracks near the bend in Kīlauea's east rift zone maintain the general strike direction of the overall rift (~65°), despite the changing orientation of the surface trace at the bend as marked by spatter cones and pit craters [*Swanson*, 2007]. The consistency of strikes and prevalence of en echelon segments in this region suggest that the overall stresses in the volcanic pile [*Dieterich*, 1988] interact with the curved rift zone to produce a combination of mode I opening and mode III shear. This combination can also be seen in models of the steady state deformation that require both deep shear and opening along the rift trace [*Owen et al.*, 2000a].

[58] Including the decollement slip in the model improves fits to the GPS sites north of the rift and on the western flank as well as coastal tilt. While the seismic response of Kīlauea's south flank to rift zone intrusions is well known [e.g., *Dvorak et al.*, 1986], this event is the first observed concurrent magmatic intrusion and slow slip event on Kīlauea [*Brooks et al.*, 2008]. Whether flank sliding is driven by magmatic intrusions or whether intrusions are driven by extensional stress from flank slip is an ongoing discussion. Both processes are likely significant in all intrusions, and many models include interactions between magmatic activity and flank motion. [*Dieterich*, 1988] for example, used numerical models to show that a feedback arises between the maximum height that magma can rise within the rift zone, fault friction, and fault width, thereby allowing fault friction to control flank slope. The interaction of the rift zone and decollement during this event suggests
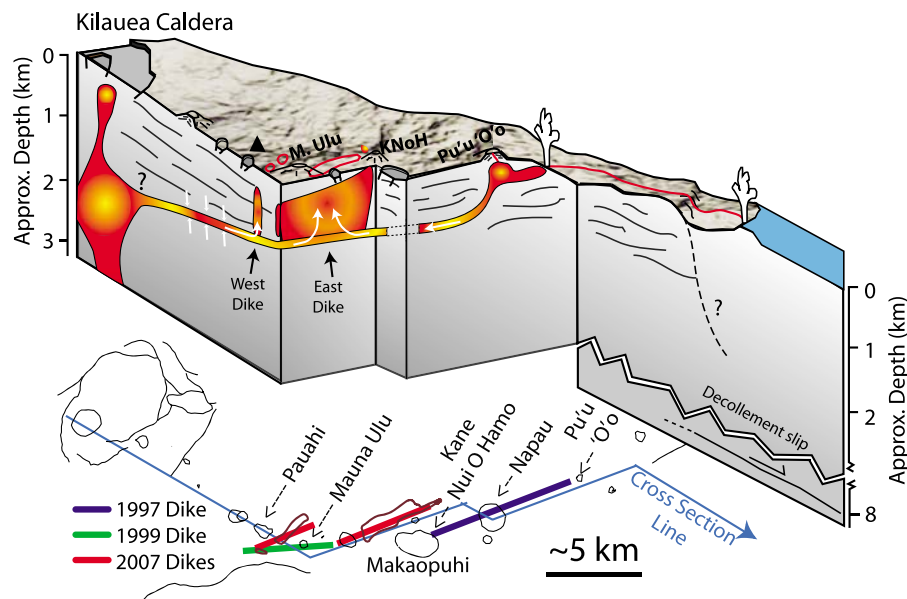
Figure 15. Schematic cross section of Kīlauea's shallow plumbing system and how it was influenced by the June 2007 intrusion. Perspective drawing is similar to that of J. Johnson (Diagram of Kilauea, 2000, Web site). Arrows show a schematic representation of magma flow during the intrusion process. Map view shown below also identifies the locations of the 1997 and 1999 intrusions.

that these processes can take place on short timescales. Indeed, *Brooks et al.* [2008] showed that the intrusion caused an increase in the Coulomb failure stress on the decollement, suggesting that the stress change led to the slow slip event.

[59] While our preferred model includes two en echelon dikes, two Mogi sources, and slip along the basal decollement, exploring simpler model spaces using MCMC methods proved useful in constraining the range of possible source geometries. The bottom depth of ~2 km, similar to those for the January 1997 (episode 54) and September 1999 intrusions [*Owen et al.*, 2000b; *Cervelli et al.*, 2002a], suggests a change from episodic to continuous deformation at this depth. A depth of ~2 km is consistent with top of the zone of neutral buoyancy postulated by *Ryan* [1988] to be the location of the active rift zone along which magma is laterally transported. Kinematic models of long-term geodetic data [e.g., *Delaney et al.*, 1990; *Cayol et al.*, 2000; *Owen et al.*, 2000a] also suggest that deformation is mostly episodic above 3 km. Interestingly, this intrusion also appears to fill a gap between the 1997 and 1999 intrusions (Figure 15). This gap was the only segment of the middle east rift zone that had not hosted an intrusion since 1983.

[60] While the January 1997, September 1999, and June 2007 dike geometries are similar, we argue that the change from deflation to inflation at Kīlauea's summit in 2003 led to increased magma pressure [*Miklius*, 2005] and hence a more forcible intrusive process. We compare observations of this intrusion to the January 1997 (episode 54) [*Owen et al.*, 2000b] and September 1999 intrusions/eruptions [*Cervelli et al.*, 2002a], which were also observed by the continuous GPS network and modeled as dikes using similar methods.

[61] We conceptualize Kīlauea's shallow plumbing since 1983 as an open magmatic system consisting of a shallow

summit magma reservoir connected via a conduit to the ERZ vents similar to *Swanson et al.*'s [1976] model for earlier eruptions. Near simultaneous tilt observations at the summit and Pu'u 'Ō'ō imply that there must be a hydraulic connection between the two [*Cervelli and Miklius*, 2003]. Although this intrusion shares the geometric similarities noted above, this intrusion occurred under different circumstances than the episode 54 and September 1999 intrusions. The episode 54 [*Owen et al.*, 2000b] and September 1999 [*Cervelli et al.*, 2002a] intrusions occurred during persistent post-1983 summit deflation. Lavas from episode 54 contained a mix of old and new magmas, suggesting that the eruption exploited long-lived magma lenses remaining in the rift zone from previous eruptions [*Thornber et al.*, 2003]. Further, episode 54 was accompanied by limited seismicity localized about the eruptive vent at Nāpau Crater. Based on these observations, [*Owen et al.*, 2000b] and [*Cervelli et al.*, 2002a] suggest that the January 1997 and September 1999 intrusions/eruptions were "passive," driven by accumulating rift extension.

[62] In contrast, the 2007 intrusion occurred during a period of inflation which began in 2003 and has been interpreted as resulting from an increase in magma supply to the volcano [*Poland et al.*, 2008a]. The June 2007 event was accompanied by more than 180 shallow M > 2 earthquakes. While the seismicity pattern of the 1999 intrusion is similar to that of the 2007 intrusion, the 1999 intrusion had fewer total earthquakes and did not reach the surface. Erupted 2007 lava is also more primitive and 30–50°C hotter than that erupted in 1997, and ~15°C hotter than episode 55 lava (erupted between 1997 and 2007 from Pu'u 'Ō'ō) [*Thornber et al.*, 2007]. We therefore classify this event as an "active" intrusion, as suggested by *Poland et al.* [2008a], implying that it was not entirely driven by passive opening of the ERZ

but was also driven by some component of magma over-pressure in the summit reservoir (Figure 15).

[63] In conclusion, the June 2007 dike event can be well modeled by ~2 m of opening on a pair of en echelon dikes. The concurrent slow slip event is similar to previous events, and produced ~15 cm of southward offshore decollement slip. The shallow magmatic system was pressurized during this event, leading to forcible intrusion of the en echelon dikes.

References

Altamimi, Z., X. Collilieux, J. Legrand, B. Garayt, and C. Boucher (2007), ITRF2005: A new release of the International Terrestrial Reference Frame based on time series of station positions and Earth Orientation Parameters, *J. Geophys. Res.*, *112*, B09401, doi:10.1029/2007JB004949.

Brooks, B. A., J. H. Foster, M. Bevis, L. N. Frazer, C. J. Wolfe, and M. Behn (2006), Periodic slow earthquakes on the flank of Kilauea Volcano, Hawai'i, *Earth Planet. Sci. Lett.*, *246*(3–4), 207–216, doi:10.1016/j.epsl.2006.03.035.

Brooks, B. A., J. Foster, D. Sandwell, C. J. Wolfe, P. Okubo, M. Poland, and D. Myer (2008), Magmatically triggered slow slip at Kilauea Volcano, Hawaii, *Science*, *321*(5893), 1177, doi:10.1126/science.1159007.

Cayol, V., and F. H. Cornet (1998), Three-dimensional modeling of the 1983–1984 eruption at Piton de la Fournaise Volcano, Réunion Island, *J. Geophys. Res.*, *103*(B8), 18,025–18,037, doi:10.1029/98JB00201.

Cayol, V., J. Dieterich, A. Okamura, and A. Miklius (2000), High magma storage rates before the 1983 eruption of Kilauea, Hawaii, *Science*, *288*(5475), 2343–2346, doi:10.1126/science.288.5475.2343.

Cervelli, P., and A. Miklius (2003), The shallow magmatic system of Kilauea Volcano, *U.S. Geol. Surv. Prof. Pap.*, *1676*, 149–163.

Cervelli, P., P. Segall, F. Amelung, H. Garbeil, C. Meertens, S. Owen, A. Miklius, and M. Lisowski (2002a), The 12 September 1999 Upper East Rift Zone dike intrusion at Kilauea Volcano, Hawaii, *J. Geophys. Res.*, *107*(B7), 2150, doi:10.1029/2001JB000602.

Cervelli, P., P. Segall, K. Johnson, M. Lisowski, and A. Miklius (2002b), Sudden aseismic fault slip on the south flank of Kilauea Volcano, *Nature*, *415*(6875), 1014–1018, doi:10.1038/4151014a.

Day, S., J. Carracedo, H. Guillou, and P. Gravestock (1999), Recent structural evolution of the Cumbre Vieja volcano, La Palma, Canary Islands: Volcanic rift zone reconfiguration as a precursor to volcano flank instability?, *J. Volcanol. Geotherm. Res.*, *94*(1–4), 135–167, doi:10.1016/S0377-0273(99)00101-8.

Delaney, P., and D. Pollard (1981), Deformation of host rocks and flow of magma during growth of minette dikes and breccia-bearing intrusions near Ship Rock, New Mexico, *U.S. Geol. Surv. Prof. Pap.*, *1212*.

Delaney, P., R. Fiske, A. Miklius, A. Okamura, and M. Sako (1990), Deep magma body beneath the summit and rift zones of Kilauea Volcano, Hawaii, *Science*, *247*(4948), 1311–1316, doi:10.1126/science.247.4948.1311.

Dieterich, J. (1988), Growth and persistence of Hawaiian volcanic rift zones, *J. Geophys. Res.*, *93*(B5), 4258–4270, doi:10.1029/JB093iB05p04258.

Dvorak, J. J., and D. Dzurisin (1997), Volcano geodesy: the search for magma reservoirs and the formation of eruptive vents, *Rev. Geophys.*, *35*(3), 343–384, doi:10.1029/97RG00070.

Dvorak, J., A. Okamura, T. English, R. Koyanagi, J. Nakita, M. Sako, W. Tanigawa, and K. Yamashita (1986), Mechanical response of the south flank of Kilauea Volcano, Hawaii, to intrusive events along the rift

systems, *Tectonophysics*, *124*(3–4), 193–209, doi:10.1016/0040-1951 (86)90200-3.

Edmonds, M., and T. Gerlach (2007), Vapor segregation and loss in basaltic melts, *Geology*, *35*(8), 751, doi:10.1130/G23464A.1.

Fiske, R., and R. Koyanagi (1968), The December 1965 eruption of Kilauea Volcano, Hawaii, *U.S. Geol. Surv. Prof. Pap.*, *607*, 1–22.

Fukuda, J., and K. Johnson (2008), A fully Bayesian inversion for spatial distribution of fault slip with objective smoothing, *Bull. Seismol. Soc. Am.*, *98*(3), 1128, doi:10.1785/0120070194.

Got, J.-L., and P. Okubo (2003), New insights into Kilauea's volcano dynamics brought by large scale relative relocation of microearthquakes, *J. Geophys. Res.*, *108*(B7), 2337, doi:10.1029/2002JB002060.

Gregorius, T. (1996), GIPSY-OASIS II: How it Works, Univ. of Newcastle upon Tyne, New Castle, U. K.

Gudmundsson, A. (2003), Surface stresses associated with arrested dykes in rift zones, *Bull. Volcanol.*, *65*(8), 606–619, doi:10.1007/s00445-003-0289-7.

Hansen, P. (1992), Analysis of discrete ill-posed problems by means of the l-curve, *SIAM Rev.*, *34*(4), 561–580, doi:10.1137/1034115.

Hansen, S., C. Thurber, M. Mandernach, F. Haslinger, and C. Doran (2004), Seismic velocity and attenuation structure of the east rift zone and south flank of Kilauea Volcano, Hawaii, *Bull. Seismol. Soc. Am.*, *94*(4), 1430–1440, doi:10.1785/012003154.

Heliker, C., and T. Mattox (2003), The first two decades of the Pu'u O'o–Kupianaha eruption: Chronology and selected bibliography, in *The Pu'u 'Ō'ō -Kupaianaha Eruption of Kīlauea Volcano, Hawai'i: The First 20 Years*, edited by C. Heliker, D. A. Swanson, and T. J. Takahashi, *U.S. Geol. Surv. Prof. Pap.*, *1676*, 1–28.

Holcomb, R. (1987), Eruptive history and long-term behavior of Kilauea Volcano, in *Volcanism in Hawai'i*, edited by R. Decker, T. Wright, and P. Stauffer, *U.S. Geol. Surv. Prof. Pap.*, *1350*, 261–350.

Liu, Y., and J. R. Rice (2007), Spontaneous and triggered aseismic deformation transients in a subduction fault model, *J. Geophys. Res.*, *112*, B09404, doi:10.1029/2007JB004930.

Metropolis, N., A. Rosenbluth, M. Rosenbluth, A. Teller, and E. Teller (1953), Equation of state calculations by fast computing machines, *J. Chem. Phys.*, *21*, 1087–1092, doi:10.1063/1.1699114.

Miklius, A. (2005), Recent inflation of Kilauea volcano during the ongoing eruption-harbinger of change?, *Eos Trans. AGU*, *86*(52), Fall Meet. Suppl., Abstract G53B-0883.

Miklius, A., P. Cervelli, M. Sako, M. Lisowski, S. Owen, P. Segal, J. Foster, K. Kamibayashi, and B. Brooks (2005), Global positioning system measurements on the island of Hawai'i: 1997 through 2004, *U.S. Geol. Surv. Open File Rep.*, *2005-1425*, 1–48.

Miyazaki, S., J. McGuire, and P. Segall (2003), A transient subduction zone slip episode in southwest Japan observed by the nationwide GPS array, *J. Geophys. Res.*, *108*(B2), 2087, doi:10.1029/2001JB000456.

Mogi, K. (1958), Relations between the eruptions of various volcanoes and the deformations of the ground surfaces around them, *Bull. Earthquake Res. Inst. Univ. Tokyo*, *36*, 111–123.

Montgomery-Brown, E., D. Sinnett, P. Segall, A. Miklius, M. Poland, and K. Larson (2007), Source models of the June 17, 2007 intrusion at Kilauea Volcano, Hawaii: Spatio-temporal evolution, *Eos Trans. AGU*, *88*(52), Fall Meet. Suppl., Abstract V52A-1138.

Montgomery-Brown, E., P. Segall, A. Miklius, P. Cervelli, and D. Shelly (2009), Kilauea slow slip events: Identification, source inversions, and relation to seismicity, *J. Geophys. Res.*, *114*, B00A03, doi:10.1029/2008JB006074.

Morgan, J., and P. McGovern (2003), Discrete element simulations of volcanic spreading: Implications for the structure of Olympus Mons, *Lunar Planet. Sci.*, *XXXIV*, Abstract 2088.

Nakamura, K. (1980), Why do long rift zones develop in Hawaiian volcanoes—A possible role of thick oceanic sediments (in Japanese), *Bull. Volcanol. Soc. Jpn.*, *25*, 255–267.

Nakata, J., and P. Okubo (2008), Hawaiian volcano observatory seismic data, January to December, 2007, *U.S. Geol. Surv. Open File Rep.*, *2008-1261*, 1–99.

Okada, Y. (1985), Surface deformation due to shear and tensile faults in a half-space, *Bull. Seismol. Soc. Am.*, *75*, 1135–1154.

Owen, S., P. Segall, M. Lisowski, A. Miklius, R. Denlinger, and M. Sako (2000a), Rapid deformation of Kilauea Volcano: Global positioning system measurements between 1990 and 1996, *J. Geophys. Res.*, *105*(B8), 18,983–18,998, doi:10.1029/2000JB900109.

Owen, S., P. Segall, M. Lisowski, A. Miklius, M. Murray, M. Bevis, and J. Foster (2000b), January 30, 1997 eruptive event on Kilauea Volcano, Hawaii, as monitored by continuous GPS, *Geophys. Res. Lett.*, *27*(17), 2757–2760, doi:10.1029/1999GL008454.

Poland, M., A. Miklius, T. Orr, A. J. Sutton, C. Thornber, and D. Wilson (2008a), New episodes of volcanism at Kilauea Volcano, Hawaii, *Eos Trans. AGU*, *89*(5), 37, doi:10.1029/2008EO050001.

Poland, M., W. Moats, and J. Fink (2008b), A model for radial dike emplacement in composite cones based on observations from Summer Coon volcano, Colorado, USA, *Bull. Volcanol.*, *70*, 861–875, doi:10.1007/s00445-007-0175-9.

Pollard, D., P. Segall, and P. Delaney (1982), Formation and interpretation of dilatant echelon cracks, *Geol. Soc. Am. Bull.*, *93*(12), 1291, doi:10.1130/0016-7606(1982)93<1291:FAIODE>2.0.CO;2.

Rivalta, E., and P. Segall (2008), Magma compressibility and the missing source for some dike intrusions, *Geophys. Res. Lett.*, *35*, L04306, doi:10.1029/2007GL032521.

Ryan, M. P. (1988), The mechanics and three-dimensional internal structure of active magmatic systems: Kilauea Volcano, Hawaii, *J. Geophys. Res.*, *93*(B5), 4213–4248, doi:10.1029/JB093iB05p04213.

Schwartz, S., and J. Rokosky (2007), Slow slip events and seismic tremor at circum-Pacific subduction zones, *Rev. Geophys.*, *45*, RG3004, doi:10.1029/2006RG000208.

Segall, P., and R. Harris (1986), Slip deficit on the San Andreas Fault at Parkfield, California, as revealed by inversion of geodetic data, *Science*, *233*(4771), 1409–1413, doi:10.1126/science.233.4771.1409.

Segall, P., E. Desmarais, D. Shelly, A. Miklius, and P. Cervelli (2006), Earthquakes triggered by silent slip events on Kilauea Volcano, Hawaii, *Nature*, *442*, 71–74, doi:10.1038/nature04938.

Shelly, D. R., G. C. Beroza, S. Ide, and S. Nakamula (2006), Low-frequency earthquakes in Shikoku, Japan, and their relationship to episodic tremor and slip, *Nature*, *442*, 188–191, doi:10.1038/nature04931.

Swanson, D. (2007), Setting of the Father's Day eruption at Kilauea, *Eos Trans. AGU*, *88*(52), Fall Meet. Suppl., Abstract V51H-08.

Swanson, D. A., W. A. Duffield, and R. S. Fiske (1976), Displacement of the south flank of Kilauea Volcano, Hawaii: The result of forceful intrusion of magma into the rift zones, *U.S. Geol. Surv. Prof. Pap.*, *963*, 1–39.

Thornber, C., T. Orr, H. Lowers, C. Heliker, and R. Hoblitt (2007), An episode 56 perspective on post-2001 comagmatic mixing along Kilauea's East Rift Zone, *Eos Trans. AGU*, *88*(52), Fall Meet. Suppl., Abstract V51H-04.

Thornber, C. R., et al. (2003), Kilauea east rift zone magmatism: An episode 54 perspective, *J. Petrol.*, *44*(9), 1525–1559, doi:10.1093/petrology/egg048.

Welstead, S. T. (1999), *Fractal and Wavelet Image Compression Techniques*, 232 pp., SPIE Opt. Eng. Press, Bellingham, Wash., doi:10.1117/3.353798.

Wilson, D., J. Uribe, S. Kamibayashi, J. Nakata, and P. Okubo (2007), Seismic characterization of the June 17, 2007 East Rift intrusion at Kilauea Volcano, *Eos Trans. AGU*, *88*(52), Fall Meet. Suppl., Abstract V51H-02.

Wolfe, C., B. Brooks, J. Foster, and P. Okubo (2007), Microearthquake streaks and seismicity triggered by slow earthquakes on the mobile south flank of Kilauea Volcano, Hawaii, *Geophys. Res. Lett.*, *34*, L23306, doi:10.1029/2007GL031625.

Yun, S.-H., P. Segall, and H. Zebker (2006), Constraints on magma chamber geometry at Sierra Negra Volcano, Galapagos Islands, based on InSAR observations, *J. Volcanol. Geotherm. Res.*, *150*, 232–243, doi:10.1016/j.jvolgeores.2005.07.009.

Zumberge, J. F., M. B. Heflin, D. C. Jefferson, M. M. Watkins, and F. H. Webb (1997), Precise point positioning for the efficient and robust analysis of GPS data from large networks, *J. Geophys. Res.*, *102*(B3), 5005–5017, doi:10.1029/96JB03860.

A. Miklius, T. Orr, and M. Poland, USGS, Hawaii Volcano Observatory, POB 51, Hawai'i National Park, HI 86718, USA.

E. K. Montgomery-Brown, P. Segall, D. K. Sinnett, and H. Zebker, Department of Geophysics, Stanford University, 397 Panama Mall, Stanford, CA 94305, USA. (emilymb1@gmail.com; dsinnett@stanford.edu)